Magnetically assembled iron oxide nanoparticle coatings and their integration with pseudo-spin-valve thin films

Chengpeng Jiang[a], Sheung Mei Ng[b], Chi Wah Leung[b] and Philip W. T. Pong[*a]

a Department of Electrical and Electronic Engineering, The University of Hong Kong, Hong Kong, China. E-mail: ppong@eee.hku.hk

b Department of Applied Physics, Hong Kong Polytechnic University, Hong Kong, China

Abstract:

The ability to prepare ordered crystalline structures by the assembly of magnetic nanoparticles is of great value for the design and fabrication of nanoparticle-based spintronics devices with novel structures and enhanced performances. In this work, nanoparticle coatings with both structural order and magnetic alignment were assembled onto flat substrates using monodisperse iron oxide nanoparticles by spin coating and heat treatment. The binary solvent mixture used as the carrier solvent for the nanoparticles enables solution-processed spin coating. The out-of-plane magnetic field applied during heat treatment promotes nanoparticle assembly. The magnetically assembled nanoparticle coating exhibits larger saturation magnetization and higher coercivity compared with its randomly aggregated counterpart, due to the easy-axis alignment and close packing of the nanoparticles. By tuning the experimental parameters, nanoparticle coatings with different morphologies were produced, in which locally ordered grains were formed due to anisotropic dipolar interactions. The potential of the nanoparticle coating for spintronic applications is demonstrated by integrating it with pseudo-spin-valve thin films, forming a nanoparticle-coated multilayer thin film structure. This composite system shows a magnetization switching behavior and spin-dependent magnetoresistance (MR) change. By decreasing the distance between the nanoparticle coating and the multilayer thin films, nanoparticle–thin film coupling and interlayer coupling were modulated, resulting in enhanced MR ratios. The presented results and proposed coupling mechanism provide insights into designing nanoparticle-based spintronic devices with enhanced performances and improved properties.

Introduction

Advances in the chemical synthesis of magnetic nanoparticles (MNPs) with uniform size and controlled shape[1–4] have enabled the self-assembly of MNPs[5–9] to build nanostructured magnetic materials with desired structures, properties, and functionalities.[5,10–12] The bottom-up self-assembly method demonstrates its potential advantages over the top-down lithography-based methods in terms of simplicity, scalability, and cost.[13] For the former, the assembled structures can be well configured by controlling their growing direction, spatial arrangement, or even spatiotemporal organization,[7,11–15] and their collective properties can also be tailored by changing the compositions or combinations of the constituent nanoparticles.[6,12,16–18] With the introduction of external stimuli (temperature, light),[5,13,19] directing fields (magnetic, flow),[10,14,19,20] directing surfaces (template, interface),[5,21,22] or interparticle interactions (chemical bonding, dipole coupling),[6,18,23,24] the self-assembly method could be appropriately employed for fabricating magnetic nanostructures composed of MNPs and could provide enhanced control over the particle placement and the structural organization.[8,10,11,14,25,26] Recently, several variants of the self-assembly strategy have been developed for MNPs, including the interfacial assembly method, evaporative assembly method, and field-directed assembly method. One example concerns the transfer of MNP monolayers from liquid sub-phase to solid surfaces using the Langmuir–Blodgett/Schaefer technique,[16,27,28] and by repeating such a process, multilayer or stratified structures can be obtained.[29,30] The second example involves the evaporative deposition of MNPs from volatile solvent onto flat substrates.[26] Using MNPs with different sizes or shapes, complex nanostructures and binary nanoparticle superlattices can be built.[8,17,31,32] Another example is related to the directional assembly of MNPs guided by an external magnetic field, producing ordered thin films,[25,33] 2D periodic patterns,[7,14,15] or 3D anisotropic superstructures.[9,19,20,33,34] From the application viewpoint, the assembled structures of MNPs with both structural order (related to packing pattern) and

magnetic alignment (associated with easy-axis orientation) are of particular interest because they could be exploited to fabricate functional magnetic materials with enhanced properties.3,5,35 However, manipulating the magnetic moment and controlling of the anisotropic energy for the MNPs in the assembled structures still remain challenging.9 In this regard, the magnetic-field directed self-assembly technique demonstrates its unique advantages,36 since the magnetization directions and collective behaviors of MNPs can be appropriately modulated under the applied magnetic field, leading to preferentially oriented magnetic dipoles.9,20,33

To be utilized for spintronic devices (such as high-density storage media,1,11 spin valve sensors,37–39 and spin transistors40–42) it is very promising if the assembled structures of MNPs (formed as homogeneous films,6,12,27,31 well-spaced arrays,7,14,22,26 or hierarchical superlattices6,8,17,31) could be further integrated with magnetic thin films due to the expectation of novel phenomena and distinctive properties resulting from spin transport and spin accumulation.3,25,35 In such MNP-based spintronic devices, the size and shape of MNPs should be precisely controlled6,31 to achieve their long-range ordered organization. The interparticle spacing and surface chemistry of MNPs should also be finely regulated1,4 since dipolar interaction and spin-dependent electron transport favor the short-range regime (within a few nanometers).18 Several works have reported the fabrication of MNP-based structures for magnetoresistance (MR) measurement, either by preparing the assembled superlattices of MNPs or by depositing MNPs as assembled films.25,32,43 Besides the progress achieved in investigating the Coulomb blockade and spin-dependent electron tunneling in these MNP-assembled superstructures,31,44 investigations on the interactions between dispersed MNPs and spin valve sensors have also been attempted for the purpose of magnetic detection and quantification.45–48 However, research works on composite systems consisting of MNPs and magnetic thin films have been scarcely reported, let alone the incorporation of assembled MNPs in spintronic devices.49,50 This is likely due to the difficulties in controlling the distance and interactions between MNPs and thin films. To address these issues, we

aimed at fabricating ordered coatings of MNPs through magnetic-field induced assembly, and depositing the MNP coatings on pseudo-spin-valve (PSV) thin films with a non-magnetic capping layer. It is believed that the close packing and magnetic alignment of the MNPs in the magnetically assembled nanoparticle coating can result in strong nanoparticle–thin film interactions. Such interactions can be appropriately tuned by altering the capping layer thickness and hence the nanoparticle–thin film distance, enabling the study of the corresponding magnetic properties and device performances of this composite system.

Herein, a new paradigm of the magnetic-field directed assembly of MNPs is developed. In this method, magnetically assembled iron oxide nanoparticle coatings were fabricated by spin coating and heat treatment. The concentration of the nanoparticle solution, the composition of the carrier solvent used for spin coating, and the magnitude of the magnetic field applied during heat treatment are well adjusted to study their influences on the coating morphology. The crystallographic orientation and the magnetic properties of the nanoparticle coating are investigated and correlated. A possible formation mechanism of the locally ordered grains in the nanoparticle coating is proposed. Furthermore, nanoparticle-coated multilayer thin film system is fabricated by preparing the nanoparticle coating on sputtered thin films with a PSV structure. The magnetization switching behavior and MR response of this system are investigated and its device performances are evaluated by tuning the distance and interactions between the nanoparticles and the thin films.

Experimental

Materials

Iron(III) oxyhydroxide (FeOOH, 99%) and oleic acid (90%) were purchased from Aldrich. Isopropyl alcohol (IPA), 1-octadecene (90%), ethanol (99.5%), acetone (99.8%), hexane, chloroform, toluene, and α-terpineol were obtained from Acros. All chemicals were used as received without further purification.

Synthesis of iron oxide nanoparticles

The synthesis of spherical iron oxide nanoparticles with a size of 12 nm follows a previously reported protocol51 that we have modified.52 In brief, a finely ground powder of FeOOH (2 mmol), oleic acid (12 mmol), and octadecene (8 ml) were added to a three-neck flask equipped with a condenser, rubber septum, thermocouple probe, heating mantle, and temperature controller. Under a blanket of Ar gas, the reaction mixture was first heated to 200 °C for 30 min at a rate of 6.6 °C min−1, and then heated to 300 °C for 1 h at a rate of 3.3 °C min−1. Mechanical stirring was applied throughout the whole reaction. By removing the heating source, the resulting black mixture was cooled to room temperature.

Purification of iron oxide nanoparticles

The solution containing iron oxide nanoparticles was first purified by adding ethanol (24 ml) and centrifuged at 5000 rpm for 5 min. The upper-layer transparent supernatant was decanted, and the remaining black slurry liquid was dissolved in chloroform (6 ml). Then, acetone (24 ml) was added, and a black-brown material was precipitated by centrifugation at 5000 rpm for 5 min. After removing the upper-layer turbid supernatant, the precipitates were dried and redispersed into chloroform (6 ml). The purification operation was repeated three more times to remove most of the physically absorbed organic surfactant, and the final precipitates were dissolved in 6 ml toluene.

Fabrication of magnetically assembled nanoparticle coatings

A nanoparticle solution suitable for spin coating was prepared beforehand. Typically, 20 μl toluene solution of iron oxide nanoparticles was diluted by adding 80 μl toluene. Afterwards, 12.5 μl of terpineol was added, and the mixture (nanoparticle concentration 2.4 mg ml−1, toluene/terpineol volume ratio 8[thin space (1/6-em)]:[thin space (1/6-em)]1) was sonicated using an ultrasonic bath and then mixed using a vortex mixer. As a result, a light-colored homogeneous solution was obtained.

The fabrication procedure of the magnetically assembled nanoparticle coating is

illustrated in Fig. 1. A silicon wafer sized at 1 cm2 with a thermally oxidized surface was sonicated in acetone, IPA, and deionized water, respectively, and then treated with HCl solution. The wafer was blown dry under N2 gas, followed by deposition of 5 μl of freshly prepared nanoparticle solution (Fig. 1a). The spin coating process was performed at 2500 rpm for 10 s with an accelerating speed of 500 rpm s−1, producing a thin layer of liquid coating on the wafer surface (Fig. 1b). Afterwards, the wafer was immediately transferred to a hot plate for heat treatment (Fig. 1c). A Petri dish was inversely capped on the wafer to minimize the air convection and ensure a controlled evaporation rate.22,52,53 The wafer was first preheated at 50 °C for 5 min, and then heated to 100 °C for 5 min to remove the low boiling-point solvent, and finally heated to 150 °C for 15 min to remove the high boiling-point solvent and surfactant. During the entire heat treatment process, a magnetic field (200 Oe) was applied perpendicular to the substrate plane to promote the nanoparticle assembly (Fig. 1c). Both the heating rate and the cooling rate were controlled at 5 °C min−1. After cooling to room temperature, a uniform coating was obtained on the wafer surface (Fig. 1d). By changing the experimental parameters, a series of samples were produced (Table 1).

Fabrication of nanoparticle-coated multilayer thin films

The multilayer thin films were designed based on a PSV structure. Si wafers with an amorphous oxide layer were loaded into a magnetron sputtering system (AJA) with a base pressure of 6 × 10−8 Torr, followed by the deposition of the multilayer structure: substrate/Ta (3.5 nm)/Co50Fe50 (12 nm)/Cu (3.5 nm)/Co50Fe50 (0.5 nm)/Ni80Fe20 (8 nm)/Ta (3 nm). The thickness of the Cu spacer has been optimized to give a large giant magnetoresistance (GMR) response. The nanoparticle coating on the multilayer thin films was prepared following the same fabrication procedure as that of the nanoparticle coating on Si described previously. The structure of the nanoparticle-coated multilayer thin film system is presented in Fig. 1e. By changing the thickness of the Ta capping layer, different samples were prepared (Table 1).

Characterization

Transmission electron microscopy (TEM) imaging was performed using a Philip CM-100 TEM operated at 100 kV. Selected area electron diffraction (SAED) patterns and high-resolution TEM images were acquired on an FEI Tecnai-F20 TEM operated at 200 kV. X-ray diffraction (XRD) patterns were collected on a Bruker D8-Advance X-ray diffractometer with Cu Kα radiation (λ = 1.5418 Å). Reflected light microscopy images were acquired using an Olympus BX-51 microscope. Scanning electron microscopy (SEM) characterization was performed on a Hitachi S-4800 SEM operated at 5 kV. Atomic force microscopy (AFM) images were recorded using a NanoScope-IV AFM operated in tapping mode. Hysteresis loop measurements were conducted on a MicroSense vibrating sample magnetometer (VSM). MR measurements were performed using a four-point probe system equipped with spring-loaded pogo pins and computer-controlled electromagnetic coils.

Results and discussion

Characterization of iron oxide nanoparticles

The morphology of the synthesized nanoparticles was characterized by TEM. As shown in Fig. 2a, the nanoparticles have a spherical shape and spontaneously form a monolayer on the surface of the TEM grid after evaporation of the solvent. The corresponding particle size histogram (inset of Fig. 2a) reveals that the nanoparticles are monodisperse with a diameter of 12.0 ± 0.9 nm. The calculated particle-size distribution (PSD) is 7%, which is close to the value (5%) reported by Colvin et al. for their 10 nm iron oxide nanoparticles.51

The structural information of the nanoparticles was obtained from both X-ray and electron diffraction patterns. Fig. 2b shows the XRD pattern of the nanoparticles, and the positions as well as the relative intensities of all the peaks can be indexed to the standard powder diffraction data of γ-Fe2O3 with a cubic spinel structure (maghemite, JCPDS #04-0755). The inset of Fig. 2b shows the SAED pattern of the nanoparticles, and the measured lattice spacing based on the diffraction rings match well with the corresponding d-spacing of the hkl planes in γ-Fe2O3. Diffraction patterns related to

the other-phase iron oxide were not observed, implying that our nanoparticles are γ-Fe2O3, in agreement with the results reported by Augustyn et al.54

The preparation of a highly stable solution of well-dispersed nanoparticles is a prerequisite for nanoparticle assembly.4,27,30 Herein, the monodisperse iron oxide nanoparticles capped by oleic acid were synthesized through the thermal decomposition of iron carboxylate salts. In the heating stage at 200 °C, iron precursors were dissolved and iron carboxylate salts were initially formed.51 In the final heating stage at 300 °C, pyrolysis of the carboxylate moieties led to the nucleation and growth of iron oxide nanocrystals.51 FeOOH was chosen as the inorganic precursor due to its low cost and non-toxicity compared with other organometallic precursors, such as Fe(CO)5, Fe(cup)3, and iron oleate.4,55–57 Octadecene was selected as the organic solvent due to its high boiling point, non-coordinating and non-polar properties, favoring the isotropic growth of spherical nanocrystals.52 Carboxylic acid with a long hydrocarbon chain was used as the surfactant, which introduces short-range steric repulsion counterbalancing van der Waals forces and prevents undesired aggregation of nanoparticles.17 Different carboxylic acids were tested for nanoparticle synthesis. Our experimental results show that oleic acid (C18H34O2) and lauric acid (C12H24O2) both resulted in monodisperse nanoparticles, but the lauric acid-capped nanoparticles exhibited a slightly wider size distribution (Fig. S1, ESI†) and poor solubility in toluene. To enable solution-processed spin coating, nanoparticles with uniform size and good solubility in organic solvents are required. Thus, the oleic acid-capped 12 nm nanoparticles with monodisperse size (PSD < 10%) were used in this work.

Characterization of nanoparticle coatings

For the magnetically assembled nanoparticle coating on Si (baseline sample NC-base), optical microscopy and SEM microscopy were employed to study its surface morphology. As shown in the optical micrograph (Fig. 3a), a homogeneous and continuous coating was formed without cracks or vacancies over hundreds of microns. The detailed nanostructure of the nanoparticle coating is depicted in the SEM image

(Fig. 3b). Uniform nanoparticles were compactly packed into locally ordered grains (similar to crystal grains). These grains sized at hundreds of nanometers are ultra-fine and highly crystalline. No bare substrate could be observed based on a large scanned area, illustrating that the nanoparticles fully covered the substrate surface as a continuous coating. The enlarged SEM image (Fig. 3c) reveals that the spherical shapes of the nanoparticles were well maintained without coalescence or deformation. The six symmetric bright spots in the fast Fourier transform (FFT) pattern of this SEM image (inset of Fig. 3c) indicate that the nanoparticles were orderly organized in a hexagonal packing pattern as an energetically favorable configuration featured by strong dipolar interactions.13,58 Individual nanoparticles are clearly resolved under SEM, confirming that most of the organic solvents and the capping ligands physically absorbed on the surface of the nanoparticles have been removed; otherwise, blurred SEM image will be obtained due to charge effect in the presence of non-conductive organics. The tilt-view SEM image (Fig. 3d, 45° tilt angle) and the cross-section TEM image (inset of Fig. 3d) briefly reflect the profiles of the locally ordered grains formed by magnetically assembled nanoparticles. The cross-section TEM image also reveals that the nanoparticle coating has an average thickness of 58 nm, and it is composed of 3 to 6 layers of the 12 nm nanoparticles. In addition, a reference sample (NC-ref) was prepared using the same fabrication procedure as that of the baseline sample (NC-base), except that no magnetic field was applied during heat treatment. Although the reference sample shows a continuous and defect-free coating, ordered packing patterns or crystalline structures are not observed and the constituent nanoparticles were randomly aggregated (Fig. S2, ESI†). Therefore, it can be inferred that the applied magnetic field promotes the formation of well-ordered structures in the nanoparticle coating.

To obtain the topological information of the magnetically assembled nanoparticle coating, AFM imaging was performed for the baseline sample (NC-base) by scanning an area of 2 μm by 2 μm. The 2D AFM image (Fig. 3e) and the 3D AFM image (Fig. 3f) both confirm that the nanoparticle coating is essentially composed of multiple

grains separated by grain boundaries. A closer observation of the grain structures reveals that they are highly crystalline with granular textures. The cross-section profile of the 2D AFM image (inset of Fig. 3e) shows obvious height difference (>30 nm) between the grain and the grain boundary, indicating that the grains may form by consuming the nanoparticles at grain boundaries.

To study the magnetic properties of the magnetically assembled nanoparticle coating, the hysteresis loop of the baseline sample (NC-base) was measured at 300 K along the out-of-plane direction (Fig. 3g and h, blue curves). As a comparison, the hysteresis loop for the reference sample (NC-ref) fabricated without any magnetic field was also measured (Fig. 3g and h, red curves). The magnetically assembled nanoparticle coating exhibits a larger magnetic coercivity (Hc = 2.1 Oe) and a higher saturation magnetization (Ms = 1.46 × 10−3 emu) compared with the randomly aggregated nanoparticle coating (Hc = 0.5 Oe, Ms = 1.33 × 10−3 emu). Note that the coercivity field is related to the energy barrier required for aligning the magnetic moments of nanoparticles upon the reversal of the magnetic field.16 The increased coercivity observed in the sample NC-base can be attributed to the increased anisotropy of the magnetically assembled structures and the enhanced dipolar interactions of the closely packed nanoparticles.34,59 Such enhanced magnetism indicates that the spatial arrangement and magnetic alignment of the nanoparticles have important influences on their collective magnetic properties.7,16 Similar findings of enhanced magnetism have been reported in our previous work, where MNPs assembled into anisotropic superstructures under the influence of a magnetic field.52 It is noteworthy that the magnetic anisotropy induced by the magnetic field in our case is along the out-of-plane direction, and it is different from the in-plane anisotropy induced by the intrinsic shape anisotropy of the nanoparticle monolayer or multilayer, as reported by Pichon's group.16,28

High-resolution TEM imaging was carried out to investigate the crystallographic orientation and easy axis direction of the magnetically assembled nanoparticles. The TEM sample was prepared by distributing the nanoparticle solution (diluted 10 times)

over a TEM grid, followed by the heat treatment process under the applied magnetic field described previously. As shown in Fig. 4, single-crystalline nanoparticles deposited on the TEM grid as a monolayer, which allows the electrons to transmit through them and enables the crystal structure of individual nanoparticles to be resolved. A lattice fringe spacing of 4.82 Å was readily measured from three nanoparticles in the scanned region, and this value corresponds to the d-spacing of the (111) plane in γ-Fe2O3 (d111 = 4.820 Å). Repeating the imaging by scanning other regions in the TEM sample also gave the result that most of the γ-Fe2O3 nanoparticles orient their [111] directions along the in-plane direction. The crystallographic orientation of the nanoparticles can be related to the magnetic-field directed assembly process. As for a γ-Fe2O3 nanoparticle with a cubic spinel crystal structure, its magnetic easy axes lie along the face diagonals, namely the [110][[1 with combining macron]10][[1 with combining macron][1 with combining macron]0][1[1 with combining macron]0] directions.60 Under an external magnetic field, the easy axis of the nanoparticle tends to align with the field direction.34,61,62 As illustrated in Fig. 4, the [111] directions of three nanoparticles are indicated by red arrows, which lie along the in-plane direction. Note that the [111] direction of the nanoparticle is orthogonal to the [[1 with combining macron]10] direction of its easy axis (inset of Fig. 4), which is inferred to be out-of-plane. This observation implies that the nanoparticles preferentially orient their easy axes along the out-of-plane direction of the applied magnetic field. It can be further deduced that a similar behavior of easy-axis alignment also exists in the samples with magnetically assembled nanoparticle coatings. Consequently, the distribution of the easy axes (magnetic anisotropy axes) of the nanoparticles is no longer random. This contributes to the increased anisotropy along the out-of-plane direction, as reflected by the enhanced magnetism shown in Fig. 3g and h.

Changing experimental parameters for nanoparticle coatings

In general, the field-directed assembly of colloidal nanoparticles on a solid surface is based on the ordering and packing of nanoparticles due to surface tension and external

field.15,23,36 Experimental parameters, including the composition of the carrier solvent, the concentration of the nanoparticle solution, and the strength of the applied field are important factors affecting the assembly process and the assembled structure.15,52

Herein, the above three experimental parameters were tuned in order to study their influences on the morphology of the magnetically assembled nanoparticle coatings. As shown in Fig. 5a and b, by changing the volume ratio of toluene to terpineol (r) in the carrier solvent, samples NC-ra1 (r = 6) and NC-ra2 (r = 4) were obtained. Locally ordered grains composed of hexagonally packed nanoparticles are observed in both samples, and these grains are similar to those found in the baseline sample (NC-base), indicating that the coating morphology is not sensitive to the solvent composition. Further reducing the solvent ratio (r = 2) resulted in nanoparticle coatings with obvious cracks at a length of hundreds of microns (Fig. S3, ESI†). As presented in Fig. 5c and d, by changing the nanoparticle concentration (c), samples NC-conc1 (c = 1.2 mg ml−1) and NC-conc2 (c = 0.6 mg ml−1) were produced. For the sample NC-conc1, a compact and continuous coating was formed, and its uniform brightness indicates that the coating surface is relatively smooth and the nanoparticles are accumulated into multilayer structures. For the sample NC-conc2, a double-layer structure is observed, with the two layers distinguished by different brightness. The bottom layer consists of highly ordered nanoparticles fully covering the substrate, whereas the top layer deposited on the bottom layer has a low coverage with the nanoparticles aggregated into irregular shapes. The coating morphologies of these two samples dramatically differ from that of the baseline sample (NC-base). This may be attributed to the nanoparticle concentration being closely related to the packing density, and different nanoparticle concentrations will lead to assembled coatings with distinct structures and thicknesses. As shown in Fig. 5e and f, by changing the magnetic field (H), samples NC-mag1 (H = 150 Oe) and NC-mag2 (H = 100 Oe) were fabricated. In both samples, locally ordered grains are not easily identified and the degree of the close packing of the nanoparticles is decreased, although continuous coatings are

formed. Such an observation implies that the strength of the applied magnetic field has a pronounced influence on the coating morphology. This is probably due to the decrease of the magnetic field compromising the magnetic alignment and ordered arrangement of the nanoparticles. It should be noted that all the experimental parameters were adjusted within appropriate ranges to produce relatively homogeneous nanoparticle coatings, considering that the nanoparticle assembly process has nonlinear dynamics.52,53

It is worth mentioning that the toluene–terpineol mixture used as the carrier solvent is crucial for preparing well-assembled nanoparticle coatings. When pure toluene was used as the solvent, a continuous coating composed of loosely aggregated nanoparticles was produced and obvious structural defects at the nano-scale were identified by SEM (Fig. S4, ESI†). The lack of highly ordered structures in this coating can be attributed to the fact that the evaporation rate of toluene was fast and thus the nanoparticles were not fully allowed to become magnetically aligned and closely packed. In another case, when pure terpineol was used as the solvent, the obtained coating is thick and non-uniform as reflected by the color variation in the optical micrograph (Fig. S5, ESI†). The corresponding surface morphology could not be detected under SEM due to the existence of organics. In contrast, by using toluene–terpineol mixture at an appropriate volume ratio, orderly assembled nanoparticle coatings were produced and the organic substances were removed.

Formation mechanism of magnetically assembled nanoparticle coatings

Considering the experimental results above, a possible formation mechanism of the magnetically assembled nanoparticle coatings can be proposed. During the spin coating process as shown in Fig. 6a, the carrier solvent containing the nanoparticles is uniformly deposited onto the substrate at room temperature. As for the carrier solvent, its viscosity and evaporation rate have been well adjusted by changing the volume ratio of toluene to terpineol. On the other hand, the remaining oleic acid dissolved in the solvent and absorbed on the nanoparticle surface acts as a surfactant, which lowers the surface tension of the carrier solvent and enhances its wetting ability on the

substrate. The subsequent heat treatment process is illustrated in Fig. 6b. Initially, at a low temperature (50 °C) and under an out-of-plane magnetic field (200 Oe), the nanoparticles in the liquid solvent are free to rotate and they tend to align their acquired magnetic moments along the field direction.61 Note that our nanoparticles are soft-magnetic iron oxide nanoparticles sized at 12 nm with single-domain property. It is reported that for a ferrite nanoparticle of ca. 10 nm and submitted to a magnetic field of 100 Oe, the Zeeman energy is of the same order of magnitude as the thermal energy at room temperature, whereas the anisotropy energy of the nanoparticle dominates over the thermal energy.61 This indicates that under a magnetic field of sufficient intensity, the nanoparticles dispersed in the solvent can rotate with their magnetic moments lying in the easy-axis direction and a preferential alignment of their easy axes can be achieved.61,62 Consequently, such easy-axis alignment of the nanoparticles promotes the field-directed assembly process. As the heating temperature increases and the carrier solvent evaporates, the nanoparticles continuously diffuse and assemble onto the solid substrate. Dipolar interaction20 and surface tension22 are the main driving forces guiding the nanoparticle assembly. Due to the anisotropic nature and the distance-dependent feature of dipolar interaction,20,28,58 the nanoparticles are developed into anisotropically shaped and hexagonally packed nanostructures, described here as locally ordered grains. Furthermore, the removal of the organic substances on the nanoparticle surface facilitates the close packing as well as enhances the dipolar interactions of the nanoparticles. As illustrated in Fig. 6c, with the complete evaporation of the liquid solvent, the locally ordered grains are fully formed by merging the free nanoparticles through diffusion and packing. These grains are isolated by grain boundaries, which are less ordered and relatively thinner. In the situation where the nanoparticle concentration is low, such grains are not fully developed due to the lack of the nanoparticles as building blocks. Instead, multilayer or monolayer structures appear as a result (Fig. 5c and d). In the situation where the magnetic field is weak, the magnetic alignment and dipolar interactions of the nanoparticles are not strong enough to produce highly ordered and well separated grains (Fig. 5e and f). Above all,

understanding the formation mechanism of the magnetically assembled nanoparticle coating is helpful for optimizing the fabrication procedure and tuning the coating morphology as desired.

Characterization of nanoparticle-coated multilayer thin films

Nanoparticle-coated multilayer thin films were fabricated by preparing a magnetically assembled nanoparticle coating on the surface of sequentially sputtered multilayer thin films (Fig. 1e). Ta is the capping layer on top of the multilayer thin films, due to its large surface energy (3.1 J m−2) compared with other capping materials (e.g., Cu: 1.8 J m−2, Au: 1.5 J m−2),63 which facilitates the wetting of liquid solvent. The multilayer thin films were designed based on a PSV structure, which is a GMR trilayer consisting of two ferromagnetic layers (hard layer, soft layer) separated by a non-magnetic spacer. In our case, 8 nm NiFe, 12 nm CoFe, and 3.5 nm Cu are the soft, hard, and spacer layer, respectively. Note that our PSV is a bottom PSV structure (hard layer at the bottom) for the purpose of investigating the interactions between the top NiFe soft layer and the soft-magnetic iron oxide nanoparticles. The 0.5 nm CoFe thin layer inserted between NiFe and Cu serves two purposes: the CoFe/Cu interface improves the GMR performance due to enhanced interfacial spin scattering, and the CoFe insertion acts as an interfacial diffusion barrier against the Ni–Cu intermixing. Besides, it is worth noting that the magnetic anisotropy of sputtered magnetic thin films favors the in-plane direction, whereas the magnetic anisotropy of our nanoparticle coating lies along the out-of-plane direction. Hence, the multilayer thin films were AC demagnetized before depositing the nanoparticle coating to reduce its magnetic interactions with the nanoparticles during fabrication.

Taking account of these conditions, a sample of nanoparticle-coated multilayer thin films (NCM-Ta3) was obtained. The SEM images (Fig. 7a and b) show that the nanoparticle coating is uniform and continuous, with the nanoparticles closely assembled into hexagonally packed structures. Locally ordered grains were not fully separated, and instead, they merged and coalesced with each other. The surface of the nanoparticle coating is quite smooth and its measured thickness is 54 nm, which

indicates that 4 to 5 layers of the nanoparticles were deposited on the multilayer thin films. The 2D AFM height image (Fig. 7c) and the 3D AFM topography image (Fig. 7d), with individual nanoparticles briefly resolved, further confirm that the coating surface is relatively flat, as reflected by a root-mean-square roughness of 4.2 nm, i.e. less than half of the nanoparticle diameter. Overall, compared with the nanoparticle coating on the Si substrate (NC-base), the nanoparticle coating on multilayer thin films (NCM-Ta3) also possesses highly ordered structures, but its surface is relatively smooth and uniform. Such differences in morphology and topology between these two samples presumably originate from the different surface properties of the receiving surfaces (amorphous silicon dioxide vs. Ta).

Magnetism of nanoparticle-coated multilayer thin films

Several works have reported the magnetic coupling in nanoparticle–thin film systems, where the nanoparticles and the thin films are in direct contact instead of being separated at a controlled distance.49,50 In our case, it is expected that the magnetic interactions between the magnetically assembled nanoparticle coating and the sputtered multilayer thin films are distance-dependent. To gain insights into this topic, three different test samples of nanoparticle-coated multilayer thin films (NCM-Ta13, NCM-Ta8, NCM-Ta3) were fabricated with different thickness of the Ta capping layer (13 nm, 8 nm, 3 nm). By changing the capping layer thickness, the magnetic coupling between the nanoparticle coating and the multilayer thin films was tuned accordingly. In addition, three control samples of pure multilayer thin films without any nanoparticle coating were fabricated with the corresponding capping layer thickness (13 nm, 8 nm, 3 nm). These control samples show the same MH curves and similar MR responses. For simplicity, the control sample with a 3 nm capping layer is used for comparison.

The magnetic properties of these samples were studied by measuring their hysteresis loops at 300 K with the magnetic field applied along the in-plane magnetic anisotropy direction of the multilayer thin films, and the MH curves are presented in Fig. 8a. The control sample exhibits a coercivity of 80 Oe and a saturation magnetization of 0.74 ×

10−3 emu, whereas the three test samples (NCM-Ta13, NCM-Ta8, NCM-Ta3) show slightly larger coercivities (80 Oe, 82 Oe, 89 Oe) and notably higher saturation magnetizations (1.43, 1.46, 1.50 × 10−3 emu). The increased saturation magnetization found in the samples of nanoparticle-coated multilayer thin films can be attributed to the magnetization contribution of the introduced nanoparticles. Besides, as the thickness of the capping layer decreases, the coercivity and the saturation magnetization gradually increase in the test samples. Such a trend can be understood by the fact that a smaller thickness of the capping layer corresponds to stronger interactions between the nanoparticle coating and the multilayer thin films, and thus the influence of the nanoparticles is more pronounced. Double-coercivity behavior is not readily identified, suggesting that the hard layer and the soft layer in our multilayer thin films are magnetically coupled with each other. Given this fact, the GMR effect and magnetization switching behavior of PSV are still observed in our samples.

The magnetotransport properties of these samples were evaluated by measuring their MR values at 300 K using the four-point probe method. An in-plane magnetic field (H) and an in-plane current (I) were applied.64 Longitudinal (H∥I) MR curves and transverse (H⊥I) MR curves were measured and compared to eliminate the anisotropic magnetoresistance (AMR) effect.65,66 The MR ratio is defined as the ratio of the resistance change when the field is present to the resistance when the field is absent: [(RH − R0)/R0] × 100%.67 As shown in Fig. 8b, the MR curves of all the samples exhibit two symmetric peaks. The resistance changes in the MR curves can be interpreted by the magnetization switching process of the multilayer thin films. The low resistance state observed at high field is due to the parallel magnetization configuration of the hard layer and the soft layer.67 The high resistance state observed at low field is attributed to the gradual switching of the soft layer magnetization and the resulting antiparallel magnetization alignment.68 The rapid drop in resistance is related to the sharp switching of the hard layer magnetization, described by the

switching field of the hard layer. The MR results indicate that the observed positive MR changes arise from the spin-dependent GMR effect and the magnetization reversal of the multilayer thin films. Besides, the magnetization switching behaviors in Fig. 8a match with the resistance changes in Fig. 8b. In particular, compared with the control sample of pure multilayer thin films which shows a switching field of 80 Oe and an MR ratio of 2.05%, all the three test samples of nanoparticle-coated multilayer thin films exhibit enhanced magnetism. As the capping layer thickness decreases (13 nm, 8 nm, 3 nm), the switching field (80, 82, 89 Oe) and the maximum MR ratio (2.08%, 2.30%, 2.62%) both increase monotonically in these test samples. The thickness-dependent magnetism enhancement of the hard-layer switching field and the MR ratio is clearly illustrated in Fig. 8c.

A possible mechanism of nanoparticle–thin film coupling (Fig. 8d) can be proposed, based on the above MH and MR results. The nanoparticles (12 nm Fe2O3 MNPs) deposited on top of the multilayer thin films demonstrate single-domain and nearly superparamagnetic behavior. Under an external magnetic field within an appropriate range (from −400 Oe to +400 Oe), the nanoparticles acquire magnetic moments along the field direction basically proportional to the field strength (Fig. 3g). The induced dipole field generated from the nanoparticles partially cancels the externally applied field in the soft layer.46 As the thickness of the capping layer decreases (from 13 nm to 3 nm), the distance between the nanoparticles and the soft layer is reduced and the magnetic interactions among them become stronger. As a result, the total magnetic field exerted on the soft layer becomes smaller due to the counteracting field introduced by the nanoparticles, and thus the interlayer coupling between the soft layer and the bottom hard layer becomes weaker. In our case, such interlayer coupling may arise from orange-peel coupling, which is highly sensitive to the surface roughness of ferromagnetic thin films.64,65,69 Since the interlayer orange-peel coupling favors the parallel magnetization configuration,69 a decline of such coupling indicates that the antiparallel magnetization configuration is enhanced. This

enhancement presumably leads to a higher switching field of the hard layer magnetization and a larger resistance change of the multilayer thin films, as reflected by a higher MR ratio. Note that the magnetization switching behavior and the MR performance in PSV devices can also be tuned by increasing the spacer thickness, which makes the soft layer–hard layer coupling less pronounced.65 However, by simply increasing the Cu spacer thickness (from 3.5 nm to 4.5 nm), a noticeable decrease of the MR ratio was observed (from 2.05% to 1.69%) in our multilayer thin films. This is probably due to the current shunting and scattering effects.65 The major advantage of introducing the nanoparticle coating over increasing the spacer thickness in the multilayer thin films is that it can provide flexibility to modulate the interlayer coupling and the magnetization configuration through the integration of the nanoparticles without changing the thickness or structure of the multilayer thin films. Herein, the above experimental results and the proposed coupling mechanism provide insights into designing and optimizing nanoparticle-based spintronic devices.

Conclusion

In summary, magnetically assembled nanoparticle coatings were prepared based on a fabrication method combining solution-processed spin coating and magnetic-field directed assembly. Using this method, monodisperse iron oxide nanoparticles were closely packed into locally ordered grains. Crystallographic analysis reveals that the nanoparticles preferentially orient their easy axes along the field direction. The characterization results indicate that the spatial arrangement and magnetic alignment of the nanoparticles have great impact on their collective magnetic properties. The experimental parameters were shown to have different effects on the coating morphology. The nanoparticle coating was further integrated with pseudo-spin-valve thin films, forming a nanoparticle-coated multilayer thin film structure. By decreasing the distance between the nanoparticles and the thin films, their magnetic interactions become more pronounced, resulting in a higher hard-layer switching field and a larger MR ratio.

The reported fabrication method provides a convenient route for depositing MNPs as

orderly assembled structures under the influence of a magnetic field.13,36 Besides, the magnetically assembled nanoparticle coating can be integrated into and interact with pseudo-spin-valve and spin-valve devices. As a result, it paves a new way to modulate the magnetoresistive properties and magnetization switching behaviors of spintronic devices, which can lead to novel device structures and greater design flexibility for magnetic sensing and storage applications.

Acknowledgements

This research was supported by the Seed Funding Program for Basic Research, Seed Funding Program for Applied Research and Small Project Funding Program from the University of Hong Kong, ITF Tier 3 funding (ITS-104/13, ITS-214/14), and University Grants Committee of HK (AoE/P-04/08). Mike Chan and Xu Li (HKU) are thanked for helpful discussions and sputtering experiments. Hon Fai Wong (PolyU) is thanked for AFM experiments. CWL acknowledges the support by PolyU (1-ZE25, G-YBJ1).

Figures & Tables

Table 1 Experimental parameters for the nanoparticle coatings (NC) and nanoparticle-coated multilayer thin films (NCM). All the samples were fabricated under the same spin coating (2500 rpm, 10 s) and heat treatment (150 °C, 15 min) conditions

Sample	Terpineol/toluene (volume ratio)	Nanoparticle concentration (mg ml^{-1})	Magnetic field (Oe)	Substrate material (thickness in nm)
NC-base	8	2.4	200	Si
NC-ref	8	2.4	0	Si
NC-ra1	6	2.4	200	Si
NC-ra2	4	2.4	200	Si
NC-conc1	8	1.2	200	Si
NC-conc2	8	0.6	200	Si
NC-mag1	8	2.4	150	Si
NC-mag2	8	2.4	100	Si
NCM-Ta3	8	2.4	200	Si/Ta 3.5/CoFe 12/Cu 3.5/CoFe 0.5/NiFe 8/Ta 3
NCM-Ta8	8	2.4	200	Si/Ta 3.5/CoFe 12/Cu 3.5/CoFe 0.5/NiFe 8/Ta 8
NCM-Ta13	8	2.4	200	Si/Ta 3.5/CoFe 12/Cu 3.5/CoFe 0.5/NiFe 8/Ta 13

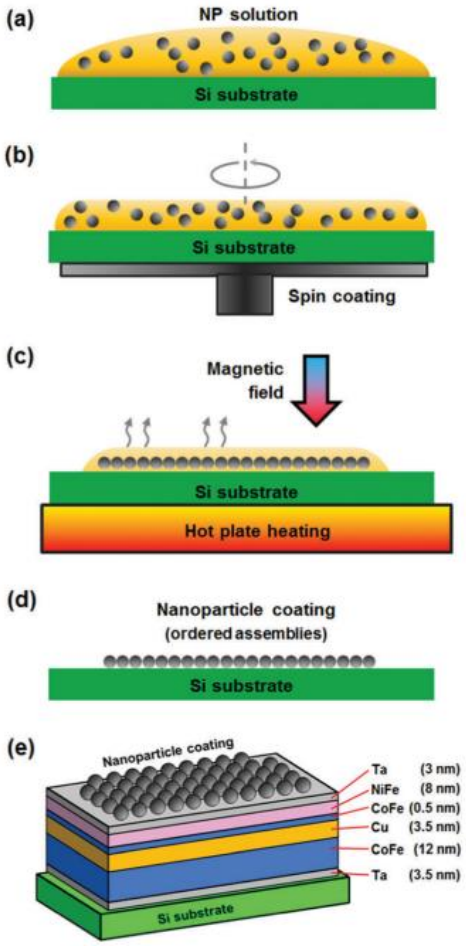

Fig. 1 Schematic illustration of the fabrication procedure of the magnetically assembled nanoparticle coating: (a) solution deposition; (b) spin coating; (c) heat treatment under applied magnetic field; (d) coating formation. (e) The structure of nanoparticle-coated multilayer thin films.

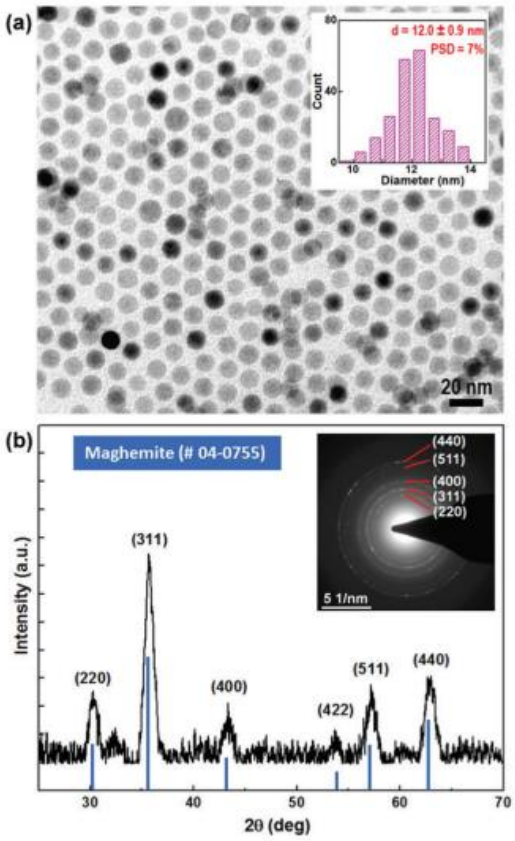

Fig. 2 (a) TEM image (inset: particle size histogram) and (b) XRD pattern (inset: SAED pattern) of the iron oxide nanoparticles.

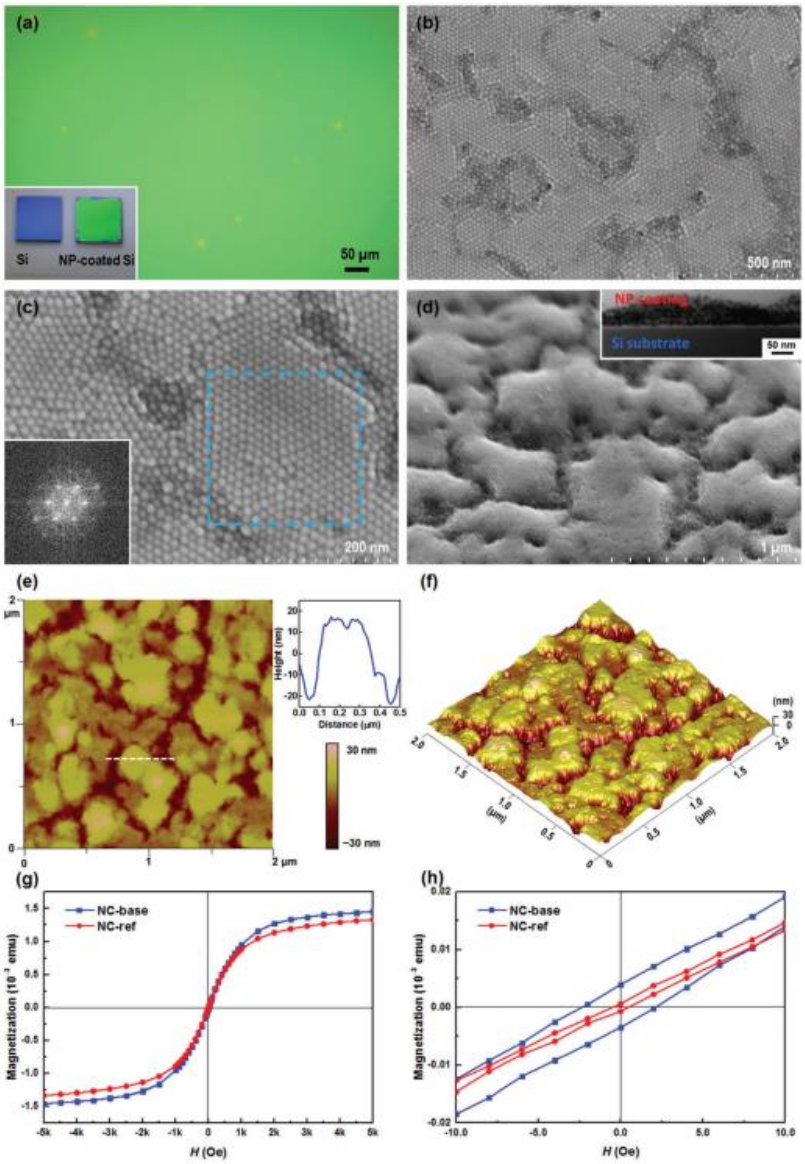

Fig. 3 (a) Optical micrograph (inset: photograph), (b) SEM image, (c) enlarged SEM image (inset: FFT pattern of the delineated region), (d) tilt-view SEM image (inset: cross-section TEM image), (e) 2D AFM height image (inset: cross-section profile extracted from the dashed line), (f) 3D AFM topography image, (g) full hysteresis loops, and (h) enlarged hysteresis loops of the magnetically assembled nanoparticle coating on Si (sample NC-base). Hysteresis loops of the randomly aggregated nanoparticle coating on Si (sample NC-ref) are also presented in (g) and (h) for comparison.

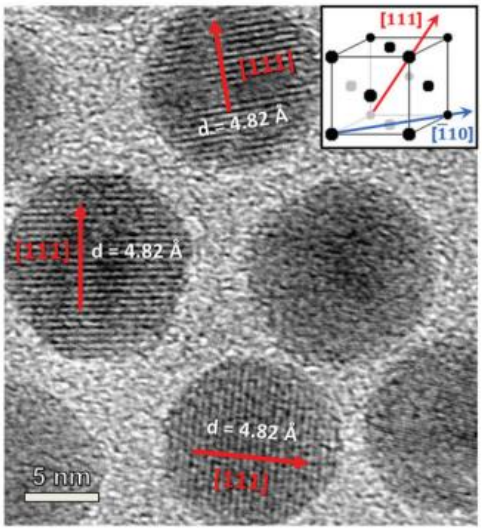

Fig. 4 High-resolution TEM image of the magnetically assembled nanoparticles showing their crystallographic orientations (inset: observed crystal direction and magnetic easy axis direction).

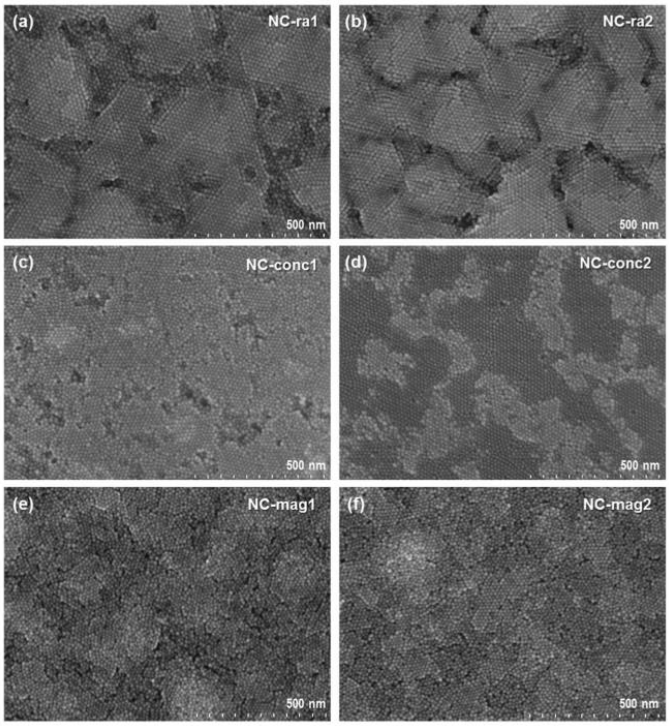

Fig. 5 SEM images of the magnetically assembled nanoparticle coatings fabricated with different experimental parameters (ratio of toluene to terpineol r, nanoparticle concentration c, magnetic field H): (a) r = 6; (b) r = 4; (c) c = 1.2 mg ml−1; (d) c = 0.6 mg ml−1; (e) H = 150 Oe; (f) H = 100 Oe. The sample name is shown in each image.

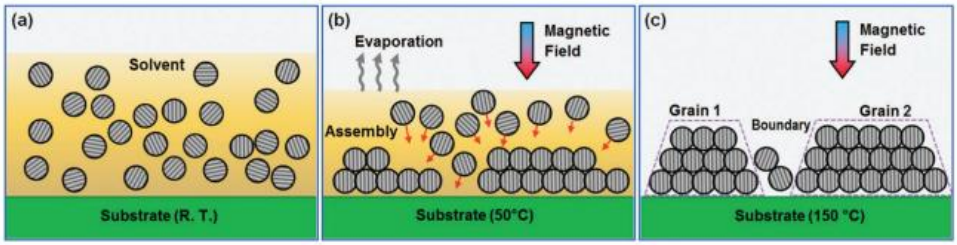

Fig. 6 Schematic illustration of the formation mechanism of the magnetically assembled nanoparticle coating: (a) deposition of nanoparticle solution; (b) magnetic-field-induced nanoparticle assembly; (c) formation of locally ordered grains. The periodic stripes within each nanoparticle represent the easy-axis direction.

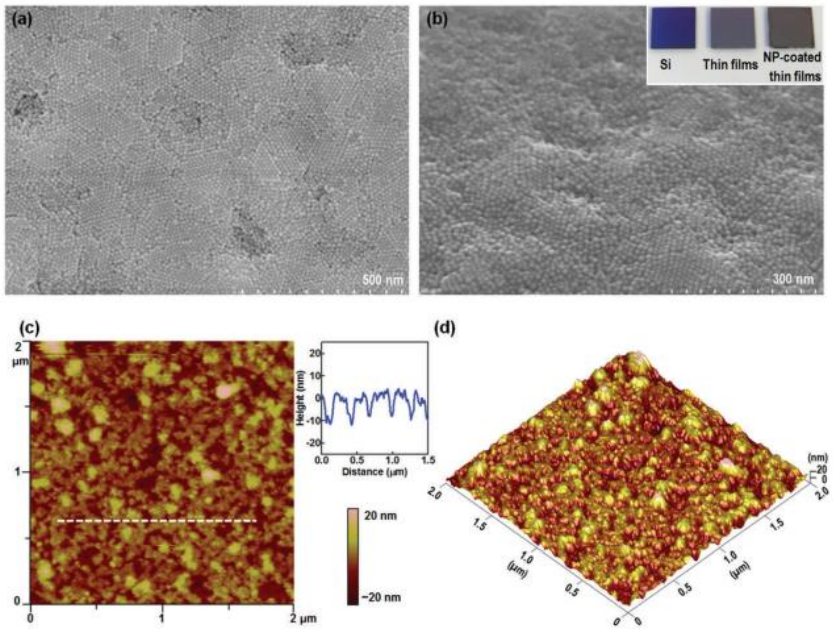

Fig. 7 (a) SEM image, (b) tilt-view SEM image (inset: photograph), (c) 2D AFM height image (inset: cross-section profile extracted from the dashed line), and (d) 3D AFM topography image of the magnetically assembled nanoparticle coating on multilayer thin films (sample NCM-Ta3).

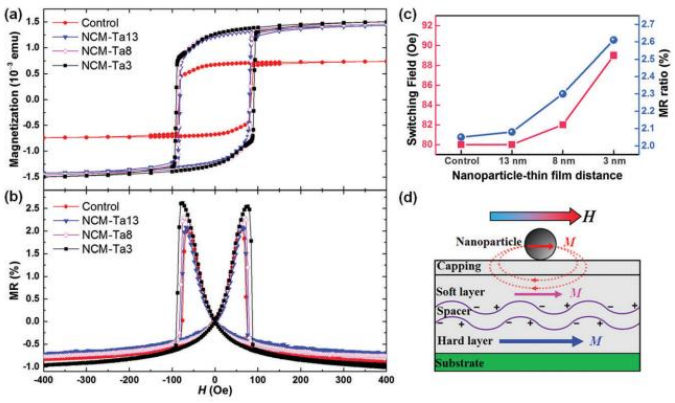

Fig. 8 (a) MH hysteresis loops and (b) MR curves of the control sample and test samples (NCM-Ta13, NCM-Ta8, NCM-Ta3). (c) Hard-layer switching fields and MR ratios of the four samples in (a) and (b). (d) A schematic illustration of the magnetic interactions between nanoparticles and multilayer thin films: M represents the magnetization; H represents the magnetic field; the dashed circles show that the induced dipole field from the nanoparticles partially cancels the applied field over the soft layer; the surface bumps (with their heights greatly exaggerated for clarity) illustrate the orange-peel coupling based on conformal roughness; the plus and minus signs represent the magnetic poles.

References

1 L. Wu, A. Mendoza-Garcia, Q. Li and S. Sun, Chem. Rev., 2016, 116, 10473–10512.

2 A. H. Lu, E. E. L. Salabas and F. Schu¨th, Angew. Chem., Int. Ed., 2007, 46, 1222–1244.

3 S. Singamaneni, V. N. Bliznyuk, C. Binek and E. Y. Tsymbal, J. Mater. Chem., 2011, 21, 16819–16845.

4 E. Wetterskog, M. Agthe, A. Mayence, J. Grins, D. Wang, S. Rana, A. Ahniyaz, G. Salazar-Alvarez and L. Bergstro¨m, Sci. Technol. Adv. Mater., 2014, 15, 5010.

5 Z. Nie, A. Petukhova and E. Kumacheva, Nat. Nanotechnol., 2010, 5, 15–25.

6 Z. Yang, J. Wei, P. Bonville and M.-P. Pileni, J. Am. Chem. Soc., 2015, 137, 4487–4493.

7 D. Toulemon, M. V. Rastei, D. Schmool, J. S. Garitaonandia, L. Lezama, X. Cattoe¨n, S. Be´gin-Colin and B. P. Pichon, Adv. Funct. Mater., 2016, 26, 2454–2462.

8 J. Brunner, I. Baburin, S. Sturm, K. Kvashnina, A. Rossberg, T. Pietsch, S. Andreev and H. Co¨lfen, Adv. Mater. Interfaces, 2016, 3, 1600431.

9 P. Tierno, Phys. Chem. Chem. Phys., 2014, 16, 23515–23528.

10 X. Xue, J. Wang and E. P. Furlani, ACS Appl. Mater. Interfaces, 2015, 7, 22515–22524.

11 B. Terris and T. Thomson, J. Phys. D: Appl. Phys., 2005, 38, R199.

12 W. Shi, R. Liang, S. Xu, Y. Wang, C. Luo, M. Darwish and S. K. Smoukov, J. Phys. Chem. C, 2015, 119, 13215–13223.

13 M. A. Boles, M. Engel and D. V. Talapin, Chem. Rev., 2016, 116, 11220–11289.

14 G. Singh, H. Chan, A. Baskin, E. Gelman, N. Repnin, P. Kra´l and R. Klajn, Science, 2014, 345, 1149–1153.

15 S. Kralj and D. Makovec, ACS Nano, 2015, 9, 9700–9707.

16 D. Toulemon, Y. Liu, X. Cattoe¨n, C. Leuvrey, S. Be´gin-Colin and B. P. Pichon, Langmuir, 2016, 32, 1621–1628.

17 D. V. Talapin, E. V. Shevchenko, M. I. Bodnarchuk, X. Ye, J. Chen and C. B.

Murray, Nature, 2009, 461, 964–967.

18 Z. Yang, J. Wei, P. Bonville and M. P. Pileni, Adv. Funct. Mater., 2015, 25, 4908–4915.

19 G. Singh, H. Chan, T. Udayabhaskararao, E. Gelman, D. Peddis, A. Baskin, G. Leitus, P. Kra´l and R. Klajn, Faraday Discuss., 2015, 181, 403–421.

20 A. Ahniyaz, Y. Sakamoto and L. Bergstro¨m, Proc. Natl. Acad. Sci. U. S. A., 2007, 104, 17570–17574.

21 M. Grzelczak, J. Vermant, E. M. Furst and L. M. Liz-Marza´n, ACS Nano, 2010, 4, 3591–3605.

22 T. Wen, D. Zhang, Q. Wen, H. Zhang, Y. Liao, Q. Li, Q. Yang, F. Bai and Z. Zhong, Nanoscale, 2015, 7, 4906–4911.

23 Y. Gao and Z. Tang, Small, 2011, 7, 2133–2146.

24 S. Kinge, T. Gang, W. J. Naber, W. G. van der Wiel and D. N. Reinhoudt, Langmuir, 2010, 27, 570–574.

25 I. C. Lekshmi, R. Buonsanti, C. Nobile, R. Rinaldi, P. D. Cozzoli and G. Maruccio, ACS Nano, 2011, 5, 1731–1738.

26 A. Dong, J. Chen, S. J. Oh, W.-K. Koh, F. Xiu, X. Ye, D.-K. Ko, K. L. Wang, C. R. Kagan and C. B. Murray, Nano Lett., 2011, 11, 841–846.

27 T. Wen and S. A. Majetich, ACS Nano, 2011, 5, 8868–8876.

28 S. Fleutot, G. L. Nealon, M. Pauly, B. P. Pichon, C. Leuvrey, M. Drillon, J.-L. Gallani, D. Guillon, B. Donnio and S. BeginColin, Nanoscale, 2013, 5, 1507–1516.

29 B. P. Pichon, C. Leuvey, D. Ihawakrim, P. Bernard, G. Schmerber and S. Begin-Colin, J. Phys. Chem. C, 2014, 118, 3828–3837.

30 B. P. Pichon, P. Louet, O. Felix, M. Drillon, S. Begin-Colin and G. Decher, Chem. Mater., 2011, 23, 3668–3675.

31 A. Dong, J. Chen, P. M. Vora, J. M. Kikkawa and C. B. Murray, Nature, 2010, 466, 474–477.

32 S. Kohiki, T. Kinoshita, K. Nara, K. Akiyama-Hasegawa and M. Mitome, ACS Appl. Mater. Interfaces, 2013, 5, 11584–11589.

33 L. Li, Y. Yang, J. Ding and J. Xue, Chem. Mater., 2010, 22, 3183–3191.

34 J.-I. Park, Y.-W. Jun, J.-S. Choi and J. Cheon, Chem. Commun., 2007, 5001–5003, DOI: 10.1039/B712513E.

35 S. Majetich, T. Wen and R. Booth, ACS Nano, 2011, 5, 6081–6084.

36 L. Hu, R. Zhang and Q. Chen, Nanoscale, 2014, 6, 14064–14105.

37 G. Li, S. Sun, R. J. Wilson, R. L. White, N. Pourmand and S. X. Wang, Sens. Actuators, A, 2006, 126, 98–106.

38 P. Freitas, R. Ferreira, S. Cardoso and F. Cardoso, J. Phys.: Condens. Matter, 2007, 19, 165221.

39 P. Braganca, B. Gurney, B. Wilson, J. Katine, S. Maat and J. Childress, Nanotechnology, 2010, 21, 235202.

40 S. Sugahara and J. Nitta, Proc. IEEE, 2010, 98, 2124–2154.

41 B. Wang, J. Wang and H. Guo, Phys. Rev. B: Condens. Matter Mater. Phys., 2003, 67, 092408.

42 P. Pfeffer and W. Zawadzki, Phys. Rev. B: Condens. Matter Mater. Phys., 2012, 86, 195303.

43 R. P. Tan, J. Carrey, M. Respaud, C. Desvaux, P. Renaud and B. Chaudret, J. Magn. Magn. Mater., 2008, 320, L55–L59.

44 R. P. Tan, J. Carrey, C. Desvaux, J. Grisolia, P. Renaud, B. Chaudret and M. Respaud, Phys. Rev. Lett., 2007, 99, 176805.

45 A. Chicharo, F. Cardoso, S. Cardoso and P. P. Freitas, IEEE Trans. Magn., 2014, 50, 1–4.

46 J. Llandro, T. Hayward, D. Morecroft, J. Bland, F. Castan˜o, I. Colin and C. Ross, Appl. Phys. Lett., 2007, 91, 203904.

47 R. S. Gaster, L. Xu, S.-J. Han, R. J. Wilson, D. A. Hall, S. J. Osterfeld, H. Yu and S. X. Wang, Nat. Nanotechnol., 2011, 6, 314–320.

48 J. D. Suh, S. D. Jung and M. A. Chung, IEEE Trans. Magn., 2009, 45, 2730–2732.

49 J. K. ne´e Moser, V. Kunej, H.-F. Pernau, E. Scheer and M. Albrecht, J. Appl. Phys., 2010, 107, 09C506.

50 G. A. B. Confalonieri, P. Szary, D. Mishra, M. J. Benitez, M. Feyen, A. H. Lu, L. Agudo, G. Eggeler, O. Petracic and H. Zabel, Beilstein J. Nanotechnol., 2010, 1, 101–

107.

51 W. Y. William, J. C. Falkner, C. T. Yavuz and V. L. Colvin, Chem. Commun., 2004, 2306–2307, DOI: 10.1039/B409601K.

52 C. Jiang, C. W. Leung and P. W. Pong, Nanoscale Res. Lett., 2016, 11, 1–12.

53 C. Jiang, L. Li and P. W. Pong, RSC Adv., 2015, 5, 98747–98756.

54 C. Augustyn, T. Allston, R. Hailstone and K. Reed, RSC Adv., 2014, 4, 5228–5235.

55 J. Park, E. Lee, N. M. Hwang, M. Kang, S. C. Kim, Y. Hwang, J. G. Park, H. J. Noh, J. Y. Kim and J. H. Park, Angew. Chem., Int. Ed., 2005, 44, 2872–2877.

56 J. Park, K. An, Y. Hwang, J.-G. Park, H.-J. Noh, J.-Y. Kim, J.-H. Park, N.-M. Hwang and T. Hyeon, Nat. Mater., 2004, 3, 891–895.

57 S. Laurent, D. Forge, M. Port, A. Roch, C. Robic, L. Vander Elst and R. N. Muller, Chem. Rev., 2008, 108, 2064–2110.

58 D. V. Talapin, E. V. Shevchenko, C. B. Murray, A. V. Titov and P. Kra´l, Nano Lett., 2007, 7, 1213–1219.

59 Y. Yu, A. Mendoza-Garcia, B. Ning and S. Sun, Adv. Mater., 2013, 25, 3090–3094.

60 J. Dormann, F. d'Orazio, F. Lucari, E. Tronc, P. Prene´, J. Jolivet, D. Fiorani, R. Cherkaoui and M. Nogues, Phys. Rev. B: Condens. Matter Mater. Phys., 1996, 53, 14291.

61 A. Ngo and M. Pileni, J. Phys. Chem. B, 2001, 105, 53–58.

62 B. Martinez, A. Roig, X. Obradors, E. Molins, A. Rouanet and C. Monty, J. Appl. Phys., 1996, 79, 2580–2586.

63 H. L. Skriver and N. M. Rosengaard, Phys. Rev. B: Condens. Matter Mater. Phys., 1992, 46, 7157–7168.

64 D. Parks, P. Chen, W. Egelhoff Jr and R. D. Gomez, J. Appl. Phys., 2000, 87, 3023–3026.

65 D. Tripathy, A. Adeyeye and S. Shannigrahi, Phys. Rev. B: Condens. Matter Mater. Phys., 2007, 75, 012403.

66 K. Matsuyama, Y. Nozaki and T. Misumi, IEEE Trans. Magn., 2001, 37, 2114–2116. 67 W. Cheng, A. Ruotolo, Y. Chan, K. Wong and C. Leung, J. Appl. Phys., 2008, 103, 103903.

68 N. Deshpande, J. Hwang, M. Seo, Y. Yoo, J. Rhee, K. Kim, Y. Shao, K. Chen, W. Pong and Y. Lee, Appl. Surf. Sci., 2014, 314, 453–457.

69 W. F. Egelhoff, R. D. McMichael, C. L. Dennis, M. D. Stiles, A. J. Shapiro, B. B. Maranville and C. J. Powell, IEEE Trans. Magn., 2006, 42, 2664–2666.